JGR Solid Earth

RESEARCH ARTICLE
10.1029/2025JB031822

Adjoint-State Attenuation Tomography: Method and Application to Northern New Zealand

Dongdong Wang[1], Jing Chen[1], Shucheng Wu[2], Tianjue Li[1], Yiming Bai[1], Yongxin Gao[3], and Ping Tong[1,4]

[1]Division of Mathematical Sciences, School of Physical and Mathematical Sciences, Nanyang Technological University, Singapore, Singapore, [2]State Key Laboratory of Geological Processes and Mineral Resources, China University of Geosciences, Wuhan, China, [3]School of Civil Engineering, Hefei University of Technology, Hefei, China, [4]Earth Observatory of Singapore, Nanyang Technological University, Singapore, Singapore

Key Points:

- A novel ray-free adjoint-state attenuation tomography method is developed and benchmarked in the Hikurangi subduction zone
- The lithosphere-asthenosphere boundary beneath the backarc is possibly characterized by contrasting high and low Q_P
- The dehydration of the deeply subducted slab contributes to the low Q_P beneath the backarc mantle wedge

Supporting Information:

Supporting Information may be found in the online version of this article.

Correspondence to:

P. Tong,
tongping@ntu.edu.sg

Citation:

Wang, D., Chen, J., Wu, S., Li, T., Bai, Y., Gao, Y., & Tong, P. (2025). Adjoint-state attenuation tomography: Method and application to northern New Zealand. *Journal of Geophysical Research: Solid Earth*, *130*, e2025JB031822. https://doi.org/10.1029/2025JB031822

Received 5 MAY 2025
Accepted 1 NOV 2025

Author Contributions:

Conceptualization: Ping Tong
Data curation: Dongdong Wang
Formal analysis: Dongdong Wang
Funding acquisition: Ping Tong
Investigation: Dongdong Wang
Methodology: Dongdong Wang, Jing Chen, Ping Tong
Project administration: Ping Tong
Resources: Dongdong Wang
Software: Dongdong Wang
Supervision: Ping Tong
Validation: Dongdong Wang
Writing – original draft: Dongdong Wang
Writing – review & editing: Dongdong Wang, Jing Chen, Shucheng Wu, Tianjue Li, Yiming Bai, Yongxin Gao, Ping Tong

Abstract We develop a novel seismic attenuation tomography method that is formulated under a matrix-free framework and avoids ray tracing. The key ingredient is the use of the adjoint-state technique to compute the gradient of the misfit function, defined as the difference between observed and synthetic t^*, to obtain an optimal attenuation model. Two advancements have been achieved over previous ray-based methods. First, t^* is accurately computed using a grid-based method to solve the Eikonal equation, followed by solving the t^* governing equation. Second, the inversion mainly requires solving the forward and adjoint equations, with a cost roughly twice that of forward modeling alone. The proposed method is benchmarked by imaging the Q_P structure of the Hikurangi subduction zone beneath northern New Zealand. The amplitude spectra of P-waves from local earthquakes are inverted to estimate t^* at 1 Hz, along with the seismic moment and corner frequency of each event. A total of 65,001 t^* measurements from 6,478 events at 44 stations are used. The new Q_P model shows high Q_P in the subducted, cold Pacific plate, adjacent to the low Q_P mantle wedge, matching previous results. Our findings reveal contrasting high and low Q_P, at depths of ~60−100 km beneath the backarc, may indicating the presence of a lithosphere-asthenosphere boundary (LAB). The low Q_P beneath the backarc originates from depths of ~150–200 km to the LAB, ascending along a nonvertical path toward the region beneath the arc, which may result from the dehydration of the deeply subducted slab.

Plain Language Summary Seismic attenuation, a key property of subsurface structures, governs the decrease in ground motion amplitude with distance from an earthquake and provides insights into variations in temperature, water content, partial melt, composition and other properties. Seismic attenuation tomography generally uses spectral decay of local earthquake waveform data to determine the underground attenuation structures. This paper presents a novel framework for seismic attenuation tomography that avoids the cumbersome ray tracing steps typically used in traditional attenuation tomography. Forward modeling is conducted using a high-precision grid-based method, whereas the inversion demands approximately twice the computational cost of forward modeling alone. The effectiveness of the developed method is demonstrated through a case study conducted in northern New Zealand. Our model reveals a gradual deepening of the lithosphere-asthenosphere boundary (LAB) from northeast to southwest beneath the backarc. In addition, we discover multiple high attenuation structures in the mantle wedge, which may characterize melts in the warm mantle beneath the backarc that feed the arc volcanoes through a non-vertically ascending path.

1. Introduction

When seismic waves, such as P and S waves, propagate outward, their amplitudes decrease due to both scattering and intrinsic attenuation (Sato et al., 2012). Scattering attenuation arises from the interaction of seismic waves with small-scale heterogeneities in the elastic properties of the medium, such as those caused by intense rock fracturing (e.g., Aki & Chouet, 1975; Sato et al., 2012). Intrinsic attenuation occurs when the kinetic energy of seismic waves is converted into thermal energy, either through internal friction along cracks or via viscoelastic deformation of the medium (e.g., Farrokhi et al., 2016; Frankel & Wennerberg, 1987). This is characterized by the total quality factor Q, which is defined as the fractional energy lost per cycle and governs the decay of the energy density spectrum over time from the earthquake's origin (Cormier, 2020). In practice, when seismic scattering is separated from absorption, the inversion yields intrinsic Q; when not separated, the inversion yields total Q. Compared to the seismic wave velocity, investigating attenuation can provide complementary insights into the

temperature, fluid content, melt, rock composition and volatile fraction of Earth's interior (e.g., Abers et al., 2014; Artemieva et al., 2004; Romanowicz & Mitchell, 2015).

Attenuation tomography is a widely used geophysical imaging technique that maps variations in the attenuation properties of subsurface earth materials. In recent years, advancements in attenuation tomography have been made in both methods and applications, including but not limited to ray-based attenuation tomography (e.g., Eberhart-Phillips & Chadwick, 2002; Wei & Wiens, 2018) and full waveform attenuation tomography (e.g., Zhu et al., 2013). Full waveform attenuation tomography, relies on solving the viscoacoustic/viscoelastic wave equation which demands significant computational resources, especially at regional or global scale. More importantly, its accuracy hinges heavily on the frequency content of the employed waveform (e.g., Karaoğlu & Romanowicz, 2018; N. Wang et al., 2023; Zhu et al., 2013). On the other hand, ray theory relies on high-frequency approximation to simplify wave equations, enabling the representation of seismic wave propagation as rays. As the most prevalent method in the past several decades, ray-based attenuation tomography, has been extensively utilized for imaging attenuation structure at subduction zones, including Tonga-Lau (e.g., Wei & Wiens, 2018; Wiens et al., 2008), western Pacific subduction zone (e.g., Liu & Zhao, 2015; Liu et al., 2014; Nakajima et al., 2013; Z. Wang & Zhao, 2019), New Zealand (e.g., Eberhart-Phillips et al., 2008, 2020), Alaska Range (Stachnik et al., 2004), Mariana arc/backarc (Pozgay et al., 2009), and Lesser Antilles arc (Hicks et al., 2023).

Ray-based attenuation tomography methods commonly use attenuation operator t^* to invert for subsurface attenuation structures. By ignoring any ray perturbation effects due to attenuation (e.g., Keers et al., 2001; Kravtsov & Orlov, 1990), t^* is computed as the integral of the reciprocal of the product of Q and velocity V along the ray path calculated in a velocity model. Therefore, accurate ray tracing is essential in ray-based attenuation tomography methods. Over the past few decades, a variety of seismic ray tracing techniques have been developed, including the widely used two-point ray tracing methods (e.g., Koketsu & Sekine, 1998; Um & Thurber, 1987) and grid-based approaches (e.g., Alkhalifah & Fomel, 2001; Rawlinson & Sambridge, 2004). Among various two-point ray tracing techniques, the pseudo-bending method (Um & Thurber, 1987) and the Thurber-modified ray-bending approach have been widely employed in attenuation tomography due to their conceptual simplicity, ease of implementation, and high computational efficiency (e.g., Eberhart-Phillips & Chadwick, 2002; Eberhart-Phillips et al., 2008; Hicks et al., 2023; Lees & Lindley, 1994; Pozgay et al., 2009; Schlotterbeck & Abers, 2001; Wei & Wiens, 2018). However, as indicated by Rawlinson et al. (2008), those two-point ray tracing methods may fail to converge to a true two-point path even in mildly heterogeneous media. Grid-based methods have become popular recently in seismic traveltime tomography due to their stability and ability to accurately determine traveltime field, even in strongly heterogeneous media (Rawlinson et al., 2010). These methods trace the ray paths from the receiver to the source by following the negative gradient of the traveltime field, which is pre-determined by numerically solving the eikonal equation (e.g., Rawlinson & Sambridge, 2004; Rawlinson et al., 2008; Zhao, 2005). It is important to note that the prediction of ray paths is not directly based on traveltime itself, but rather on the traveltime gradient. The grid-based fast sweeping method developed by D. Wang, Chen, Hao, and Tong (2025) enables the accurate computation of t^* based on the traveltime gradient, without the need for ray tracing, thereby capable of enhancing the accuracy of attenuation tomography.

Similar to most traveltime inversions, the inversion scheme for seismic attenuation tomography usually requires computing the gradient of the misfit function (also known as the Fréchet derivative). In ray-based attenuation tomography methods, calculating the Fréchet derivative typically involves ray tracing, followed by the construction and solution of the Fréchet derivative matrix. The adjoint-state technique, an elegant and physically insightful mathematical technique, efficiently computes the Fréchet derivative, making it a popular choice for solving the seismic inverse problem (e.g., Fichtner et al., 2006; Plessix et al., 2000; Tarantola, 1984; Tromp et al., 2005). In seismic traveltime tomography, employing the adjoint-state technique avoids the need for ray tracing and directly computes the Fréchet derivative matrix, making the associated cost equivalent to twice the solution of the forward-modeling problem (Taillandier et al., 2009). The adjoint-state method has been applied in local-body wave tomography using absolute traveltimes, without (e.g., Leung & Qian, 2006; Taillandier et al., 2009; Tong, 2021a) or with (e.g., Tong, 2021b; J. Chen, Chen, et al., 2023) considering anisotropy, as well as differential traveltime tomography (Tong et al., 2024), joint transmission and reflection traveltime tomography (e.g., Rawlinson & Sambridge, 2004; ; J.-W. Huang & Bellefleur, 2012), teleseismic traveltime tomography (J. Chen, Wu, et al., 2023), slope tomography (F. Tavakoli et al., 2017), and surface wave traveltime tomography (Hao et al., 2024).

To leverage the high-accuracy numerical solver, specifically the fast sweeping method, for calculating t^* and the efficiency of the adjoint-state technique, we aim to reformulate the theoretical framework of the ray-based attenuation tomography and develop an adjoint-state attenuation tomography method. The developed method is benchmarked by inverting the Q_P structure of the Hikurangi subduction zone beneath northern New Zealand using local P-wave t^* data. The remaining content of this article is organized as follows. In Section 2, we present the theoretical framework of adjoint-state attenuation tomography, including the derivation of the governing equation for t^*, the Fréchet derivative, the model parameterization, and the optimization algorithm. In Section 3, we present the application in northern New Zealand including the data preparation, the starting model and earthquake locations, the inverted results, and discussion. Finally, we provide the conclusions in Section 4.

2. Adjoint-State Attenuation Tomography

2.1. Governing Equation for t^*

Let us denote the propagation velocity of the seismic wave under consideration (either P or S) by $v(\boldsymbol{x})$. The traveltime t from the source to the receiver can be calculated by integrating the reciprocal of velocity along the curved ray path connecting them

$$t = \int_L \frac{1}{v(\boldsymbol{x})} \mathrm{d}l, \tag{1}$$

where $\mathrm{d}l$ is the arclength along the ray path L. In the context of wave propagation, Q, the quality factor, is a dimensionless parameter. We commonly use the reciprocal of the quality factor, that is, $1/Q$, to denote the attenuation of seismic waves, which is proportional to the amount of energy lost per cycle of wave propagation. Thus, a high Q indicates low attenuation, while a low Q indicates high attenuation. As demonstrated by Keers et al. (2001), when attenuation is small ($1/Q \ll 1$), ray paths are hardly affected by the attenuation. The attenuation operator t^* can be expressed by (e.g., Stachnik et al., 2004; Wei & Wiens, 2018)

$$t^* = \int_L \frac{1}{Q(\boldsymbol{x})v(\boldsymbol{x})} \mathrm{d}l. \tag{2}$$

Equations 1 and 2 can be expressed as the following directional derivatives,

$$\frac{dt}{dl} = \frac{1}{v(\boldsymbol{x})}, \tag{3}$$

and

$$\frac{dt^*}{dl} = \frac{1}{Q(\boldsymbol{x})v(\boldsymbol{x})}. \tag{4}$$

Mathematically, considering the relation between the directional derivative and the gradient, for Equations 3 and 4, we can respectively obtain

$$\frac{dt}{dl} = \nabla t(\boldsymbol{x}) \cdot \frac{\boldsymbol{l}}{|\boldsymbol{l}|}, \tag{5}$$

$$\frac{dt^*}{dl} = \nabla t^*(\boldsymbol{x}) \cdot \frac{\boldsymbol{l}}{|\boldsymbol{l}|}, \tag{6}$$

where $\boldsymbol{l}/|\boldsymbol{l}|$ denotes the unit tangent vector along the ray path direction, ∇t and ∇t^* indicate the gradients of t and t^*, respectively. It is worth emphasizing that the same unit vector $\boldsymbol{l}/|\boldsymbol{l}|$ in Equations 5 and 6 explicitly indicates the same propagation direction for t and t^*. In an isotropic medium, the unit tangent vector $\boldsymbol{l}/|\boldsymbol{l}|$ is equivalent to the unit normal of the wavefront

$$\frac{\boldsymbol{l}}{|\boldsymbol{l}|} = \frac{\nabla t(\boldsymbol{x})}{|\nabla t(\boldsymbol{x})|}. \tag{7}$$

For simplicity, in the following derivations, we define $s(\boldsymbol{x})$ (slowness) as $1/v(\boldsymbol{x})$ and $q(\boldsymbol{x})$ as $1/Q(\boldsymbol{x})$. According to Equations 3, 5, and 7, the Eikonal equation, which governs the wavefront propagating from point source $\boldsymbol{x}_s$ to any position $\boldsymbol{x}$ with a boundary condition, can be derived as

$$\nabla t(\boldsymbol{x}) \cdot \nabla t(\boldsymbol{x}) = s^2(\boldsymbol{x}), \quad t(\boldsymbol{x}_s) = 0. \tag{8}$$

It should be noted that Equation 8 can also be derived from the wave equation under high frequency approximation (Shearer, 2019). Combining Equations 4 and 6–8, we can derive

$$\nabla t(\boldsymbol{x}) \cdot \nabla t^*(\boldsymbol{x}) = q(\boldsymbol{x}) s^2(\boldsymbol{x}), \quad t^*(\boldsymbol{x}_s) = 0. \tag{9}$$

So far, we have established the governing Equation 9 that describes the accumulation of t^* from point source $\boldsymbol{x}_s$ to any position $\boldsymbol{x}$.

2.2. Fréchet Derivative

For seismic P- or S-waves originating from the earthquake location $\boldsymbol{x}_{s,n}$ $(n = 1, 2, \ldots, N)$ within an Earth volume Ω, t^* governed by Equation 9 can be expressed as follows, with the corresponding boundary condition at the source location,

$$\nabla t_n(\boldsymbol{x}) \cdot \nabla t_n^*(\boldsymbol{x}) = q(\boldsymbol{x}) s^2(\boldsymbol{x}), \quad t_n^*(\boldsymbol{x}_{s,n}) = 0. \tag{10}$$

For Equation 10, the boundary $\partial\Omega$ includes the Earth's surface. A total of M stations, located at $\boldsymbol{x}_{r,m}$ $(m = 1, 2, \ldots, M)$, are installed to record seismic waveforms from these earthquakes. During the inversion, we aim to find an optimized model parameter $q(\boldsymbol{x})$ that minimizes the difference between the observed t^{*o} and the synthetic t^*. Here, we use the least squares objective function to quantify the misfit function,

$$\chi[q(\boldsymbol{x})] = \frac{1}{2} \sum_{n=1}^{N} \sum_{m=1}^{M} w_{n,m} \left[t_n^*(\boldsymbol{x}_{r,m}) - t_n^{*o}(\boldsymbol{x}_{r,m}) \right]^2. \tag{11}$$

The weighting $w_{n,m}$ can be adjusted based on the quality and existence of the associated $t_n^{*o}(\boldsymbol{x}_{r,m})$.

We then derive an expression for Fréchet derivative of the objective function $\chi[q(\boldsymbol{x})]$ with respect to $q(\boldsymbol{x})$. It should be noted that the slowness of P-wave or S-wave keeps unchanged in the following derivations. By assigning an infinitesimal perturbation $\delta q(\boldsymbol{x})$ to $q(\boldsymbol{x})$, a corresponding small perturbation $\delta t_n^*(\boldsymbol{x})$ will be generated in $t_n^*(\boldsymbol{x})$. As discussed in Section 2.1, attenuation has a negligible effect on the travel path at seismic frequencies, and thus we can assume that the perturbation $\delta q(\boldsymbol{x})$ does not affect the traveltime $t_n(\boldsymbol{x})$, given a fixed slowness. Accordingly, Equation 10 with its boundary condition for the perturbed attenuation model $q(\boldsymbol{x}) + \delta q(\boldsymbol{x})$ writes

$$\nabla t_n(\boldsymbol{x}) \cdot \nabla \left[t_n^*(\boldsymbol{x}) + \delta t_n^*(\boldsymbol{x}) \right] = s^2(\boldsymbol{x}) [q(\boldsymbol{x}) + \delta q(\boldsymbol{x})], \quad t_n^*(\boldsymbol{x}_{s,n}) + \delta t_n^*(\boldsymbol{x}_{s,n}) = 0. \tag{12}$$

Subtracting Equation 10 from Equation 12 yields

$$\nabla t_n(\boldsymbol{x}) \cdot \nabla \delta t_n^*(\boldsymbol{x}) = s^2(\boldsymbol{x}) \delta q(\boldsymbol{x}), \quad \delta t_n^*(\boldsymbol{x}_{s,n}) = 0. \tag{13}$$

Similarly, with such infinitesimal perturbation $\delta q(\boldsymbol{x})$, the perturbation in the objective function Equation 11 is

$$\begin{aligned}\delta\chi[q(\boldsymbol{x})] &= \sum_{n=1}^{N}\sum_{m=1}^{M} w_{n,m}\left[t_n^*(\boldsymbol{x}_{r,m}) - t_n^{*o}(\boldsymbol{x}_{r,m})\right]\delta t_n{}^*(\boldsymbol{x}_{r,m}) \\ &= \sum_{n=1}^{N}\int_{\Omega}\sum_{m=1}^{M} w_{n,m}\left[t_n^*(\boldsymbol{x}) - t_n^{*o}(\boldsymbol{x}_{r,m})\right]\delta t_n{}^*(\boldsymbol{x})\delta(\boldsymbol{x}-\boldsymbol{x}_{r,m})\,\mathrm{d}\boldsymbol{x}.\end{aligned} \tag{14}$$

We now introduce an arbitrary test function $P_n(\boldsymbol{x})$. Multiplying $P_n(\boldsymbol{x})$ on both sides of Equation 13 and integrating the Earth's volume Ω, we can obtain

$$\int_{\Omega} P_n(\boldsymbol{x})\nabla t_n(\boldsymbol{x})\cdot\nabla\delta t_n^*(\boldsymbol{x})\mathrm{d}\boldsymbol{x} = \int_{\Omega} P_n(\boldsymbol{x})s^2(\boldsymbol{x})\delta q(\boldsymbol{x})\mathrm{d}\boldsymbol{x}. \tag{15}$$

By introducing the following product rule for differentiation

$$\nabla\cdot\left[P_n(\boldsymbol{x})\nabla t_n(\boldsymbol{x})\delta t_n^*(\boldsymbol{x})\right] = P_n(\boldsymbol{x})\nabla t_n(\boldsymbol{x})\cdot\nabla\delta t_n^*(\boldsymbol{x}) + \delta t_n^*(\boldsymbol{x})\nabla\cdot[P_n(\boldsymbol{x})\nabla t_n(\boldsymbol{x})], \tag{16}$$

to Equation 13 and applying the divergence theorem, we can derive

$$\int_{\partial\Omega}\boldsymbol{n}\cdot\left[P_n(\boldsymbol{x})\nabla t_n(\boldsymbol{x})\delta t_n^*(\boldsymbol{x})\right]\mathrm{d}\boldsymbol{x} - \int_{\Omega}\delta t_n^*(\boldsymbol{x})\nabla\cdot[P_n(\boldsymbol{x})\nabla t_n(\boldsymbol{x})]\,\mathrm{d}\boldsymbol{x} = \int_{\Omega} P_n(\boldsymbol{x})s^2(\boldsymbol{x})\delta q(\boldsymbol{x})\mathrm{d}\boldsymbol{x}. \tag{17}$$

We assume that the test function at the boundary $\partial\Omega$ satisfies

$$P_n(\boldsymbol{x}) = 0, \quad \boldsymbol{x}\in\partial\Omega. \tag{18}$$

Then, inserting Equation 18 into Equation 17 and combining all the events n ($n = 1,2,\ldots,N$), one can derive

$$\sum_{n=1}^{N}\int_{\Omega} P_n(\boldsymbol{x})s^2(\boldsymbol{x})\delta q(\boldsymbol{x})\mathrm{d}\boldsymbol{x} - \sum_{n=1}^{N}\int_{\Omega}\delta t_n^*(\boldsymbol{x})\nabla\cdot[P_n(\boldsymbol{x})\,\nabla(-t_n(\boldsymbol{x}))]\,\mathrm{d}\boldsymbol{x} = 0. \tag{19}$$

Comparing Equations 14 and 19, we further assume that the test function $P_n(\boldsymbol{x})$ satisfies

$$\nabla\cdot[P_n(\boldsymbol{x})\,\nabla(-t_n(\boldsymbol{x}))] = \sum_{m=1}^{M} w_{n,m}\left[t_n^*(\boldsymbol{x}) - t_n^{*o}(\boldsymbol{x}_{r,m})\right]\delta(\boldsymbol{x}-\boldsymbol{x}_{r,m}). \tag{20}$$

Then, Equation 14, the perturbation of the objective function $\delta\chi[q(\boldsymbol{x})]$, which depends on the relative attenuation model perturbation, $\delta q(\boldsymbol{x})/q(\boldsymbol{x})$, can be expressed as

$$\delta\chi[q(\boldsymbol{x})] = \sum_{n=1}^{N}\int_{\Omega} P_n(\boldsymbol{x})s^2(\boldsymbol{x})\delta q(\boldsymbol{x})\mathrm{d}\boldsymbol{x} = \int_{\Omega} K_q(\boldsymbol{x})\frac{\delta q(\boldsymbol{x})}{q(\boldsymbol{x})}\mathrm{d}\boldsymbol{x}, \tag{21}$$

where

$$K_q(\boldsymbol{x}) = \sum_{n=1}^{N} K_{q,n}(\boldsymbol{x}) = \sum_{n=1}^{N} P_n(\boldsymbol{x})s^2(\boldsymbol{x})q(\boldsymbol{x}). \tag{22}$$

Here $K_q(\boldsymbol{x})$ is the Fréchet derivative of the objective function $\chi[q(\boldsymbol{x})]$ with respect to $q(\boldsymbol{x})$, which is also called the sensitivity kernel. $K_{q,n}(\boldsymbol{x})$ is the n-th event kernel. For a specific event n recorded by station m, we define its kernel as the individual kernel.

Equation 20 is a transport equation and also called the adjoint equation, and $P_n(\boldsymbol{x})$ represents the adjoint field. The source term is represented by the residual $t_n^*(\boldsymbol{x}_{r,m}) - t_n^{*o}(\boldsymbol{x}_{r,m})$ on the right-hand side of Equation 20, which arises from the discrepancy between the true attenuation model and the attenuation model used to calculate the synthetic

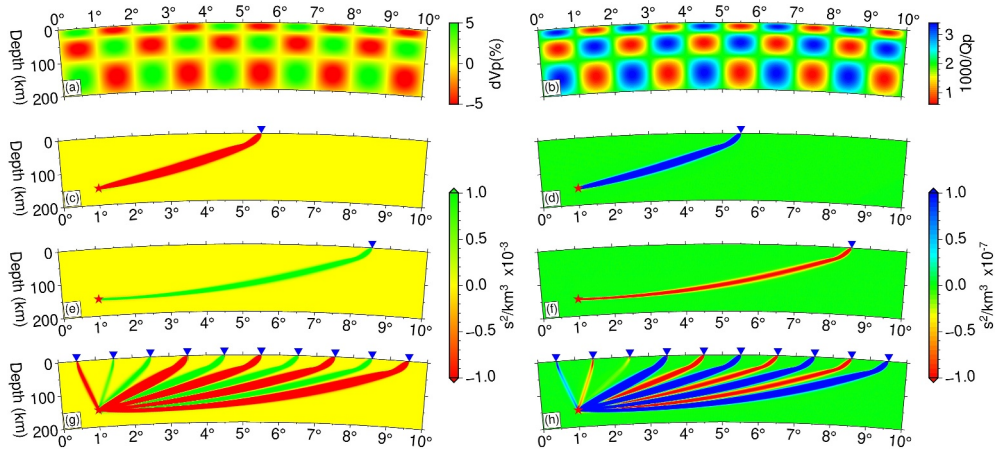

Figure 1. Comparison of the sensitivity kernels for adjoint-state traveltime tomography (left column) with that in adjoint-state attenuation tomography (right column). The relative velocity perturbation $\Delta v(\boldsymbol{x})/v_0(\boldsymbol{x})$ shown in (a), defined with respect to a vertically increasing background velocity model $v_0(\boldsymbol{x})$, is used to construct the perturbed velocity model $v_0(\boldsymbol{x})+\Delta v(\boldsymbol{x})$ for computing the observed t^o. The attenuation model $Q(\boldsymbol{x})$ shown in (b), generated by superimposing the positive and negative anomalies onto a uniform background model ($1000.0/Q_P = 2.0$) and the fixed $v_0(\boldsymbol{x})$ are used to compute the observed t^{*0}. Kernels for traveltime tomography are computed using $v_0(\boldsymbol{x})$, whereas those for attenuation tomography use the same $v_0(\boldsymbol{x})$ along with a uniform attenuation model ($1000.0/Q_P = 2.0$). (c)–(f) display individual kernels for adjoint-state traveltime (c and e) and attenuation (d and f) tomography, whereas (g) and (h) illustrate event kernels for each method.

$t_n^*(\boldsymbol{x}_{r,m})$. The scalar field $P_n(\boldsymbol{x})$ on the left-hand side of Equation 20 is generated by back-transporting the residual $t_n^*(\boldsymbol{x}_{r,m}) - t_n^{*o}(\boldsymbol{x}_{r,m})$ at each receiver to the source location along the direction $\nabla(-t_n(\boldsymbol{x}))$. For a specific event n, $P_n(\boldsymbol{x})$ can be determined by solving Equation 20 considering the summation of the residuals of t^* at all stations as the source term.

In Figure 1, we illustrate an individual kernel and an event kernel for attenuation tomography (right panel), and compare them with those in traveltime tomography (left panel). The details of calculating kernels in adjoint-state traveltime tomography can be found in Tong (2021a). Steps for calculating kernels in the attenuation tomography can be summarized in the following three steps: (a) The traveltime field $t(\boldsymbol{x})$ is computed by solving the Eikonal equation (Equation 8) using the fast sweeping method (Zhao, 2005). (b) Using the calculated traveltime field $t(\boldsymbol{x})$, the field $t^*(\boldsymbol{x})$ is computed by solving Equation 9 using a modified fast sweeping method. The implementation details of this method are described in D. Wang, Chen, Hao, and Tong (2025); (c) the adjoint field $P_n(\boldsymbol{x})$ can then be computed by the fast sweeping method (Leung & Qian, 2006) according to Equation 20 and the misfit kernel is determined by solving Equation 22. The sign of each individual kernel is determined by the traveltime residual $t_n(\boldsymbol{x}_{r,m}) - t_n^o(\boldsymbol{x}_{r,m})$ for traveltime tomography (Figures 1c, 1e, and 1g) and the residual $t_n^*(\boldsymbol{x}_{r,m}) - t_n^{*o}(\boldsymbol{x}_{r,m})$ for attenuation tomography (Figures 1d, 1f, and 1h), both measured at seismic stations. It should be noted that the individual kernel has a certain width due to the numerical approximation on a discretized grid. Comparing the traveltime tomography (left panel) with the attenuation tomography (right panel), we observe that for the same event-station pair, the individual kernels have the same shape. This arises because the left-hand side of the adjoint equation in attenuation tomography (Equation 20) has the same form as that in traveltime tomography, differing only in their source terms (residuals). Furthermore, the event kernel can be calculated by summing all individual kernels related to the same event (Figures 1g and 1h).

The derivation of the adjoint-state attenuation tomography follows a similar approach to that used in adjoint waveform tomography (Tromp et al., 2005) and adjoint-state traveltime tomography (Tong, 2021a). It can be considered as an alternative to the first arrival attenuation tomography developed by X. Huang et al. (2020), who use the Lagrangian multiplier approach. However, there are several key differences between this approach and the method outlined in X. Huang et al. (2020): (a) t^* is defined as $t^* = \int_L 1/(Q(\boldsymbol{x})v(\boldsymbol{x}))\mathrm{d}l$ rather than $t^* = \int_L \pi/(Q(\boldsymbol{x})v(\boldsymbol{x}))\mathrm{d}l$, to keep compatible with that used in the measurement of t^* (Section 3.2.2); (b) the relative perturbation $\delta q(\boldsymbol{x})/q(\boldsymbol{x})$ is inverted rather than $\delta q(\boldsymbol{x})$. Based on this, the sensitivity kernel derived above has a different mathematical expression compared to that in X. Huang et al. (2020); (c) A newly developed modified fast sweeping algorithm is used to solve Equation 9 (D. Wang, Chen, Hao, & Tong, 2025). (d) we apply

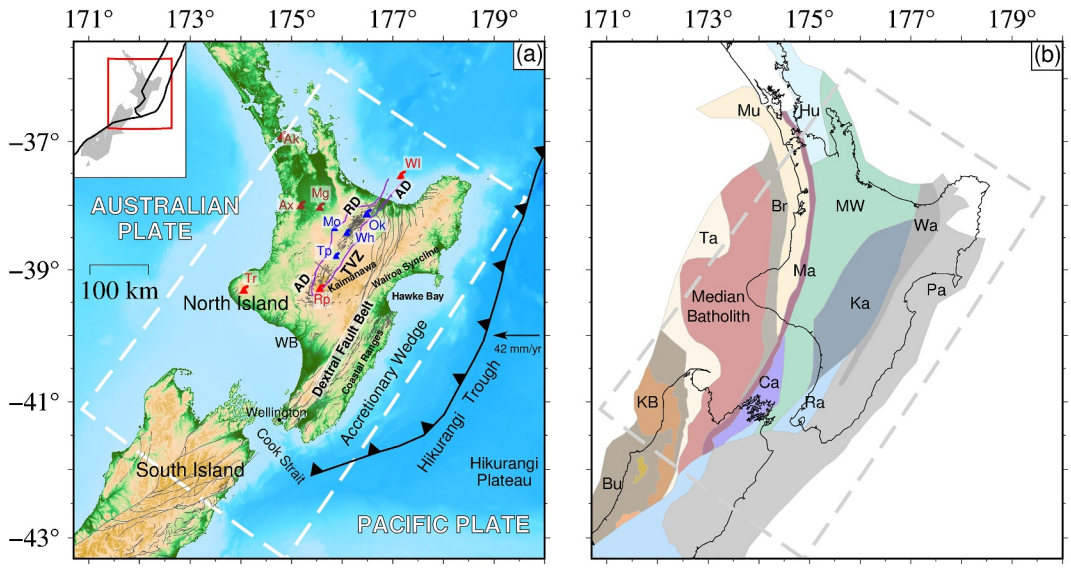

Figure 2. (a) Location and topography of North Island and north of South Island, New Zealand, superposed by major tectonic features. Boundary of the Australian Plate in the northwest and the Pacific Plate in the southeast is indicated by the trench. Major faults are shown in gray lines. The research region is indicated by the white dashed line. The Taupō Volcanic Zone (TVZ), marked by the purple line, is divided into three distinct segments: andesite-dominant (AD) cone volcanoes in the northern and southern segments, and rhyolite-dominant (RD) caldera volcanoes (shown in solid gray) in the central segment (Wilson et al., 1995). Volcanism by caldera (blue triangles), active andesite volcanoes (red triangles), and non-silicic (brown triangles). Volcanic labels: Ak, Auckland; Ax, Alexandra; Mg, Maungataurari; WI, White Island; Ok, Okataina; Rp, Ruapehu; Tr, Taranaki; Mo, Mangakino; Wh, Whakamaru; Tp, Taupō.(b) Basement geological terranes, after Mortimer (2004). Terranes: Pahau (Pa), Rakaia (Ra), Waioeka (Wa), Kaweka (Ka), Hunua Waipapa (Hu), Morrinsvile Waipapa (MW), Media Batholith (MB), Karamea batholith (KB), Brook Street (Br), Buller (Bu), Caples (Ca), Maitai (Ma), Murihiku (Mu) and Takaka (Ta).

the developed adjoint-state attenuation tomography method in large-scale seismological imaging studies and consider the spherical coordinates (Figure S1 in Supporting Information S1), which naturally take the Earth's curvature into consideration.

2.3. Model Parameterization and Optimization Algorithm

After computing the sensitivity kernel for $q(\boldsymbol{x})$, we iteratively update the attenuation model using the multiple-grid parameterization (Tong et al., 2019) and the step size-controlled gradient descent method (Tong, 2021a) until the misfit function stabilizes or converges. The core idea of the multiple-grid parameterization is to construct subsurface models on several non-overlapping grids in a staggered manner, with the average of these models serving as the output attenuation model at every iteration (Tong et al., 2019). The key advantage of using the multiple-grid approach is its implicit smoothing regularization on sensitivity kernels, which helps reduce artificial anomalies caused by subjective inversion grid selection. Damping regularization is implicitly applied during the implementation of the step size-controlled gradient descent method. Specifically, the parameter perturbation is constrained within ±20.0% of the current attenuation model, and the step size is dynamically adjusted based on the trajectory of the misfit function. During the inversion, the adjoint-state method enables computation of the misfit function gradient without the need to construct, store, or solve the Fréchet matrix, which is required in traditional ray-based attenuation tomography methods.

3. Application: Tomography of Northern New Zealand

3.1. Background and Motivation

The Hikurangi subduction zone in northern New Zealand is selected as the test site to assess the real-world performance of the proposed method (Figure 2a). On one hand, this region exhibits particularly interesting tectonic features: it lies along the convergent boundary between the Pacific and Australian plates (Figure 2a). The convergence, occurring at a rate of approximately 42 mm yr^{-1} (DeMets et al., 1994), exhibits high obliquity, with

margin-perpendicular motions primarily accommodated by the westward subduction of the Hikurangi Plateau. The active tectonics of the North Island are dominated by subduction at the Hikurangi Trough, backarc rifting in the Taupō Volcanic Zone (TVZ), and strike-slip faulting in the eastern North Island dextral fault belt (Figure 2a). The dipping seismic zone related to the subducted plate has a strike of N40°E (Ansell & Bannister, 1996), and extends to more than 300 km depth beneath the western part of the backarc region. The basement terranes of northern New Zealand, overlain by the tectonic overprints of the Haast Schist (modified after Mortimer (2004)), are shown in Figure 2b. On the other hand, this region has good data coverage (Section 3.2.1) and has been the focus of extensive research on velocity and attenuation tomography, resulting in the well-established New Zealand-Wide 2.3 (NZ-Wide 2.3) model (Eberhart-Phillips et al., 2022). This model provides a valuable reference for selecting the initial model and facilitates meaningful comparison with our results.

3.2. Data Preparation

3.2.1. Data Collection

Waveform data are collected from the New Zealand permanent network (GeoNet; www.geonet.org.nz; Gale et al., 2015; Petersen et al., 2011). This network, coded as "NZ," comprises 54 stations uniformly distributed in North Island and northern South Island. A catalog of P wave arrival times, local magnitudes (M_L), and earthquake locations is also downloaded from GeoNet (GNS Science, 1970). Earthquakes occurring between January 2000 and January 2023 in the study region, with M_L ranging from 3.0 to 6.5, are selected. To reduce the impact of near-surface complexities on wave propagation (e.g., Hicks et al., 2023; Pozgay et al., 2009; Stachnik et al., 2004; Wei & Wiens, 2018), we require earthquake depths to be greater than 10 km. After applying these selection criteria, 145,690 earthquakes are selected.

3.2.2. Inversion for Source Parameters and t^*

We investigate path-averaged attenuation by inverting for $t^* = t/Q$ from the amplitude spectra of P waves. The method used to estimate t^* follows a workflow similar to that of Hicks et al. (2023), which has been developed over decades and employed in several prior studies (e.g., Pozgay et al., 2009; Rychert et al., 2008; Stachnik et al., 2004; Wei & Wiens, 2018). Previous researches indicate that Q exhibits a weak dependence on frequency within the seismic frequency band, a relationship often expressed as

$$Q(f) = Q_0 f^{\alpha}, \tag{23}$$

where Q_0 is the quality factor at a reference frequency of 1 Hz, and α is a universal frequency-dependence exponent (Romanowicz & Mitchell, 2015). The frequency-dependence attenuation operator $t^*(f)$ can be expressed as

$$t^*(f) = t_0^* f^{-\alpha}, \tag{24}$$

where $t_0^* = t/Q_0$ describing the attenuation operator at 1 Hz. Incorporating Equation 24, the displacement amplitude spectrum $A_{mn}(f_i)$ for the n-th ($n = 1, 2, \ldots, N$) earthquake recorded by the m-th ($m = 1, 2, \ldots, M$) station can be fitted by (e.g., Boatwright, 1978; Lees & Lindley, 1994; Lindley & Archuleta, 1992; Wei & Wiens, 2018)

$$A_{mn}(f_i) = \frac{C_{mn} M_{0n} e^{-\pi f_i^{1-\alpha} t^*_{0mn}}}{1 + (f_i/f_{cn})^2}, \tag{25}$$

where f_i is the i-th sampled frequency. C_{mn} is a frequency-independent constant coefficient for a specific event-station ($n - m$) pair, which can be estimated with an approximation that accounts for the effects of geometrical spreading, free surface, and a spherically averaged radiation pattern (Aki & Richards, 2002). M_{0n} and f_{cn} are respectively the seismic moment and the corner frequency of event n. t^*_{0mn} describes t^* at 1 Hz for event n and station m. C_{mn} corrections are estimated using a 1-D velocity model (Figure S2 in Supporting Information S1) obtained by laterally averaging the NZ-Wide 2.3 velocity model for northern New Zealand. Based on

Equation 25, the non-negative least squares algorithm is employed to solve for t^*_{0mn}, as well as M_{on} and f_{cn} for each event. The procedures for determining t^* can be summarized as the following three steps:

Step 1: Estimation of the seismic moment M_0

We transform local magnitude M_L to moment magnitude M_W using a relationship derived from the regression analyses for New Zealand and its adjacent offshore area (Ristau, 2013),

$$M_L = \begin{cases} 0.93\ M_W + 0.54, & \text{if} \quad h \le 33\ \text{km} \\ M_W - 0.94e^{\frac{-h}{75.37}} + 0.8, & \text{otherwise,} \end{cases} \tag{26}$$

where h is the focal depth in km. Then, the seismic moment M_0 can be calculated using a relationship (Aki & Richards, 2002),

$$\log_{10} M_0 = 1.5\ M_W + 9.095. \tag{27}$$

Step 2: Determination of the corner frequency f_c

By taking the natural logarithm of Equation 25, it can be rewritten as

$$\ln\left[A_{mn}\left(f_i\right)\right] + \ln\left[1 + \left(f_i/f_{cn}\right)^2\right] - \ln C_{mn} - \ln M_{0n} = -\pi f_i^{1-\alpha} t^*_{0mn}. \tag{28}$$

Assuming a circular rupture, the corner frequency f_c can be expressed using the empirical relationship (Anderson, 1986)

$$f_c = 0.49\beta\left(\frac{\Delta\sigma}{M_0}\right)^{\frac{1}{3}}, \tag{29}$$

where β is the shear-wave velocity at the hypocenter, $\Delta\sigma$ is the stress drop, and M_0 is determined in *Step* 1. The upper and lower bounds of $\Delta\sigma$ are 60 and 1 Mpa (Abercrombie, 1995; Eberhart-Phillips et al., 2014), respectively, and these values are used to establish reasonable upper and lower limits for f_c.

We then employ the grid search method over the range of f_c to find the best fitting f_c and t^* by minimizing the residuals of observed and theoretical spectrum based on solving Equation 28. For each earthquake, a minimum of four high-quality spectral observations is necessary to determine f_c (Hicks et al., 2023). A t^* measurement is considered acceptable if its spectral misfit is less than 20.0 %. In Figure 3, we present an example illustrating the fitting process for an earthquake that occurred at a depth of 124 km and was recorded at stations located in the backarc, volcanic arc, and forearc regions. The vertical component of P-wave signal is windowed for 5 s starting at the picked arrival time, while the noise is windowed for the same duration immediately preceding the signal window (Figure 3c). The multitaper approach is adopted to compute signal and noise spectra (Prieto, 2022). The frequency range employed for inversion is determined by the widest bandwidth where the signal-to-noise ratio exceeds 2.0, with a minimum frequency bandwidth of 2 Hz. The assumed shear wave velocity β and the seismic moment M_0 determined by Equation 27 may introduce significant uncertainties, and then generate some unreasonable f_c by Equation 29. However, the broad range of stress drop ensures that the f_c range determined by Equation 29 can include all potential values. We use a modest frequency exponent $\alpha = 0.27$, according to previous laboratory experiments (Jackson et al., 2002; Jackson & Faul, 2010).

Step 3: Inversion for the attenuation operator t^*

After the first round of inversion (*Step* 2), f_c is well determined. We then compare the observed spectrum with the synthetic spectrum calculated using the inverted f_c and t^* values. For the second round of inversion, which yields the final t^* results, we retain only the event-station pairs with a well-fitting spectrum, discarding those with a poor fit. This round has the same process with the f_c inversion (*Step* 2). During the inversion, we also take the frequency-dependent site effects into consideration. We employ the strategy of computing the residual spectra to determine site effects (e.g., Hicks et al., 2023; Stachnik et al., 2004; Wei & Wiens, 2018). For each event-station

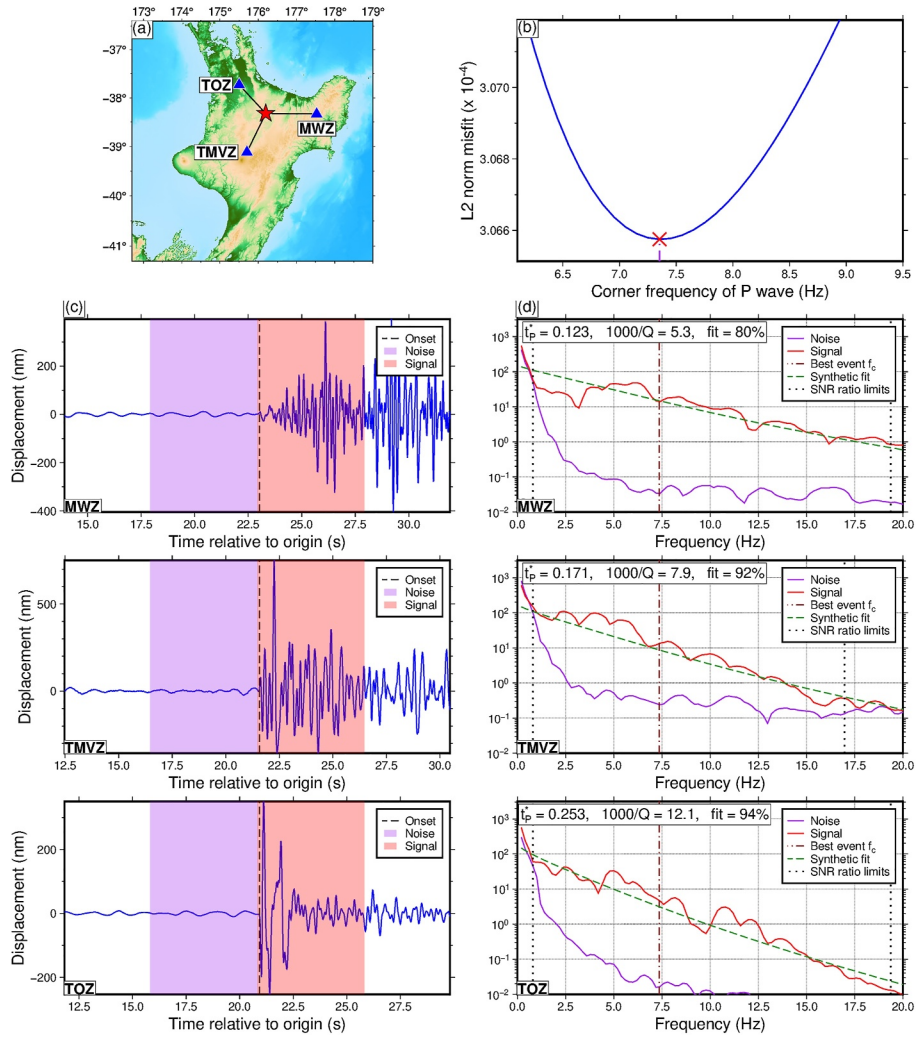

Figure 3. Example of f_c inversions for an M_L 4.1 event occurred on 2015-05-14T09:04:29 and located at 38.32°S 176.20°E with a depth of 124 km. (a) The locations of event and stations, with corresponding waveforms and spectra plotted in (c) and (d). Station MWZ is located in the forearc, TMVZ is on the volcanic arc, and TOZ is in the backarc. (b) Misfit of the t^* inversion as a function of P-wave corner frequency. The red cross indicates the best-fitting corner frequency f_c used for computing t^*. (c) and (d) respectively show the displacement waveforms (left panel) and spectra (right panel) recorded by the three representative stations. In (d), t_P^* and $1000/Q$ represent the inverted attenuation operator and the path-averaged attenuation (scaled for amplification), respectively, for specific event–station pair. "fit" refers to the agreement between the observed P-wave spectra and the corresponding synthetic spectra.

pair, the residual spectrum can be characterized by the difference between the observed and synthetic spectra, which are respectively calculated by the left and right-hand sides of Equation 28. The residual spectra for each station over all events are averaged and smoothed to generate the site effects (Figure S3 in Supporting Information S1). After subtracting the site effects from the original signal spectrum, the final t_0^* value can be obtained by conducting the t_0^* inversion process again. We find that the final t_0^* measurements only exhibit slight changes compared to those determined without removing the site effects. Using the previous inversion workflow and eliminating unrealistic values, we have successfully compiled a database of well-fitting t_0^* values, consisting of 97,512 observations from 13,299 events.

3.2.3. Data Filtering

The research region is delineated by the white dotted line in Figure 2. To save computational cost, we set the reference location at 39.7°S and 175.0°E and rotate the research region to a regular domain within the range of

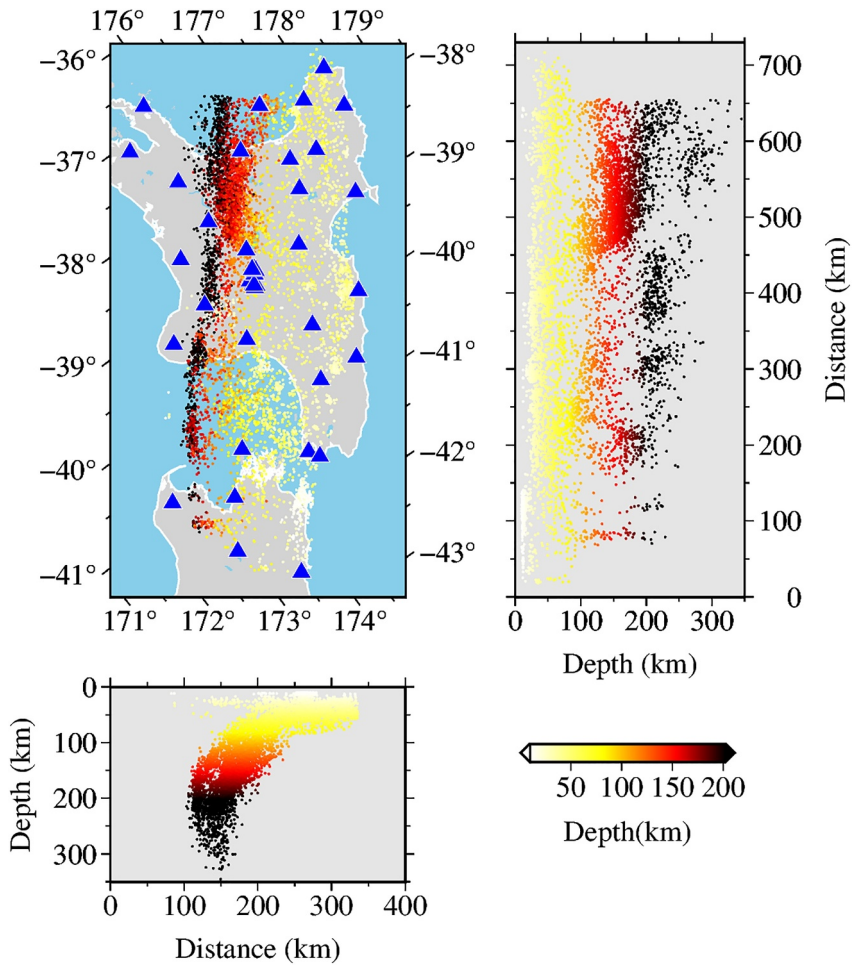

Figure 4. The spatial distributions of events (colorcoded by depth) and seismic stations (blue triangles). The final retained P-wave t^* values, obtained from the spectra of the earthquakes recorded by the seismic stations, are used to perform the attenuation tomography.

$[-1.7°, 2.0°] \times [-3.0°, 4.0°]$. In the vertical direction, it is from 4.0 km above the sea level to 370.0 km below the sea level. t^* data obtained in Section 3.2.2 is then filtered for the subsequent attenuation tomography. To avoid event clustering, we partition the study region into small blocks with sizes of $0.007° \times 0.007° \times 0.2$ km. In each small block, we only keep one event with the maximum number of t^*. Each event is required to have at least four t^* measurements. Each station is required to have at least ten t^* measurements, and earthquakes located outside the seismic network are excluded. As a result, a total of 65,001 P-wave t^* from 6,478 earthquakes and 44 stations are chosen.

3.3. Starting Model and Earthquake Locations

A good starting model is essential for the convergence of tomographic inversion. The v_P model derived from the NZ-Wide 2.3 model is selected as the velocity model and remains unchanged throughout the inversion. The initial attenuation model is a 1-D Q_P model (Figure S2 in Supporting Information S1) obtained by laterally averaging the NZ-Wide 2.3 model. All 6,478 earthquakes are relocated using the eikonal equation-constrained earthquake location method (Tong, 2021a) based on the 3-D v_P model. It should be noted that the locations of these earthquakes remain unchanged during the attenuation inversion process. The distributions of the stations and the relocated earthquakes are shown in Figure 4.

3.4. Results and Discussion

We perform checkerboard resolution tests (CRTs) to evaluate the resolving capability of t^* data and the robustness of the tomographic inversion. A dense forward grid with a size of 0.023° × 0.023° × 2.42 km is used to represent the 3-D model. Five sets of inversion grids, positioned in a staggered way along the $\phi-$, $\theta-$, and $r-$ directions, are used to assemble the model parameters (Figure S4 in Supporting Information S1). The inversion grid is defined with a spacing of 0.264° in both the ϕ and θ directions. Vertically, the grid nodes for one set of inversion grids are placed at depths of 0.0, 10.0, 20.0, 35.0, 50.0, 70.0, 90.0, 115.0, 140.0, 170.0, 200.0, 235.0, 270.0, 310.0, and 350.0 km. The CRTs show that the geometry of staggered anomalies is satisfactorily recovered, suggesting that the measured t^* data are capable of revealing Q_P heterogeneity in northern New Zealand (Figures S5–S8 in Supporting Information S1). The details for CRTs can be found in Supporting Information S1. During the inversion, we treat the 44 stations as sources and the 6,478 earthquakes as receivers, based on the reciprocity principle. This strategy requires performing only 44 forward and adjoint simulations per iteration, rather than 6,478. We carry out 80 iterations on the National Supercomputing Center (NSCC) Singapore's HPC platform using 44 processors powered by AMD EPYC 7713 64-core CPUs at 2.0 GHz, completing the inversion in approximately 260.0 min.

The same inversion strategy as the CRTs is implemented, but real t^* data is used to image the Q_P structures. After 80 iterations, the final Q_P model is obtained, with the objective function decreasing by 82.45%, from 272.96 s^2 to 47.89 s^2. To achieve a better illustration, the Q_P anomalies are presented using $\log_{10}$ scaling. Map views of the inverted Q_P model are shown in Figure 5, while cross-sections of the Q_P model are displayed in Figure 6. To assess the influence of the velocity model on the inversion results, we also perform an inversion using an initial 1-D v_P model (Figure S2 in Supporting Information S1). As shown in Figures S9 and S10 in Supporting Information S1, the main patterns of high and low Q_P anomalies remain largely consistent, with only slight differences in amplitude between the inversion using 1-D or 3-D v_P model, indicating that artifacts due to velocity model dependency are likely minimal. Below, we first benchmark the developed adjoint-state attenuation tomography method by comparing the inverted Q_P results with NZ-Wide 2.3 model. Then, we discuss the Q_P model of this study and provide interpretations to the new features.

3.4.1. Comparison With NZ-Wide 2.3 Model

When comparing, note that our Q_P is frequency-dependent with a reference of 1 Hz and $\alpha = 0.27$ (Equations 23–25), while NZ-Wide 2.3 model uses 10 Hz and $\alpha = 0.50$ (Eberhart-Phillips et al., 2022). Stachnik et al. (2004) indicates that variations in reference frequency and α can modify path-averaged Q_P measurements, ultimately affecting the inverted Q_P. Based on the results from Stachnik et al. (2004), we can infer that the path-averaged Q_P determined with a reference frequency of 10 Hz and $\alpha = 0.50$ is higher than that obtained with a reference frequency of 1 Hz and $\alpha = 0.27$ in the mantle wedge. This is probably the main reason why our Q_P in the mantle wedge is distinctly lower than that of NZ-Wide 2.3 model (Figure 7). To clearly compare these Q_P anomalies, we use different scales for display to highlight the patterns (Figure 7 and Figures S11–S17 in Supporting Information S1).

The patterns of the 3-D Q_P models are comparable, even when different reference frequencies and α are adopted (Figure 7 and Figures S11–S17 in Supporting Information S1). For example, at 26-km depth, the entire TVZ region exhibits low Q_P, extending from the northeastern boundary near White Island (WI) volcano to the southwestern boundary beyond Ruapehu (Rp) volcano, with similarly low Q_P observed in the northeastern North Island and Coastal Ranges (Figure 5a and Figures S11a and S11b in Supporting Information S1). The southwestern North Island, beneath Taranaki (Tr) and offshore, exhibits a moderate to high Q_P feature from depths of 26–40 km, extending southward into the northern South Island at around 65 km depth (Figure 5 and Figure S11 in Supporting Information S1). In both models, the slab is well imaged with high Q_P (Figure 6 and Figures S14–S17 in Supporting Information S1). At depths of 65–160 km, the slab deflects to the southwest, which is consistent with the Q_S results from Eberhart-Phillips et al. (2020) (Figures 5c–5f and Figures S12 and S13 in Supporting Information S1). This deflection is interpreted as a result of the deeply subducted Hikurangi Plateau, particularly in the southwest of North Island (e.g., Eberhart-Phillips et al., 2008, 2020). The boundary between high Q_P slab and low Q_P mantle wedge below 100-km depth (Figure 6 and Figures S14–S17 in Supporting Information S1) closely aligns with the slab interface model of Williams et al. (2013). Both models show the mantle wedge characterized by low Q_P, with our models revealing more complex low Q_P features (Figure 7 and Figures S14–S17 in Supporting Information S1), which will be discussed in detail in Section 3.4.3.

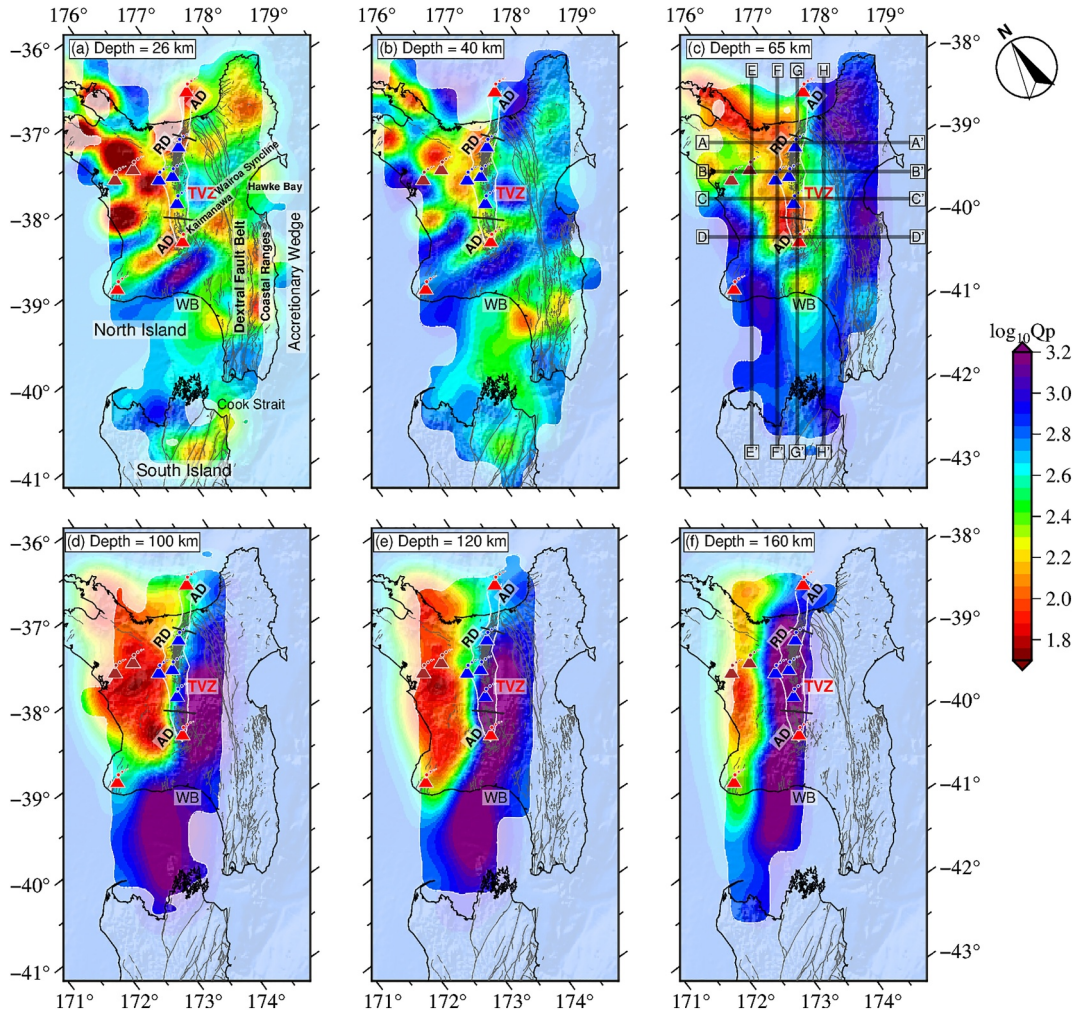

Figure 5. Map views of the final 3-D Q_P model at six representative depths, ranging from 26 to 160 km. Thin gray lines denote active faults, while thin white line marks the TVZ region. The locations of eight cross-sections are shown in (c). The interpretable region is defined by the CRTs.

3.4.2. The Backarc Lithosphere-Asthenosphere Boundary (LAB)

From northwest to southeast beneath the backarc, a new distinct feature is a depth-increasing boundary between high and low Q_P, which is absent in NZ-Wide 2.3 model (Figure 7). Such boundary is located at a depth of ~60 km in Profile B-B′ (Figure 6b), ~75 km in Profile C-C′ (Figure 6c), and ~90 km in Profile D-D′ (Figure 6d). Profile E-E' (Figure 6e) shows that this boundary can extend to depths exceeding ~100 km in the southern part of the North Island. The restoration test demonstrates that this boundary is well resolved, rather than being an artifact of smearing (Figure 8). Additionally, even when using a 1-D initial v_P model, the boundary persists in the results, further demonstrating its robustness (Figures S9 and S10 in Supporting Information S1).

According to the receiver function (RF) results from Horspool et al. (2006), the lithosphere beneath the backarc in the western North Island is estimated to have a thickness of 75 km (Eberhart-Phillips et al., 2020). Buffett et al. (2025) identify a negative velocity discontinuity west of Taupō at a depth of 62 ± 8 km and interpreted it as the LAB. These RF estimates are broadly consistent with the boundary between high and low Q_P anomalies observed in our results. Romanowicz and Mitchell (2015) indicate that the ductile asthenosphere is usually more attenuating than the lithosphere, and variations in attenuation are crucial for identifying changes in the LAB. Hence, we interpret the sharp Q_P boundary beneath the backarc as the LAB. The variation in LAB depth from northeast to southwest may be attributed to highly delamination and thinning of the mantle lithosphere on the northern side (e.g., Dimech et al., 2017; Stern et al., 2013). Also supported by RF results, a negative velocity

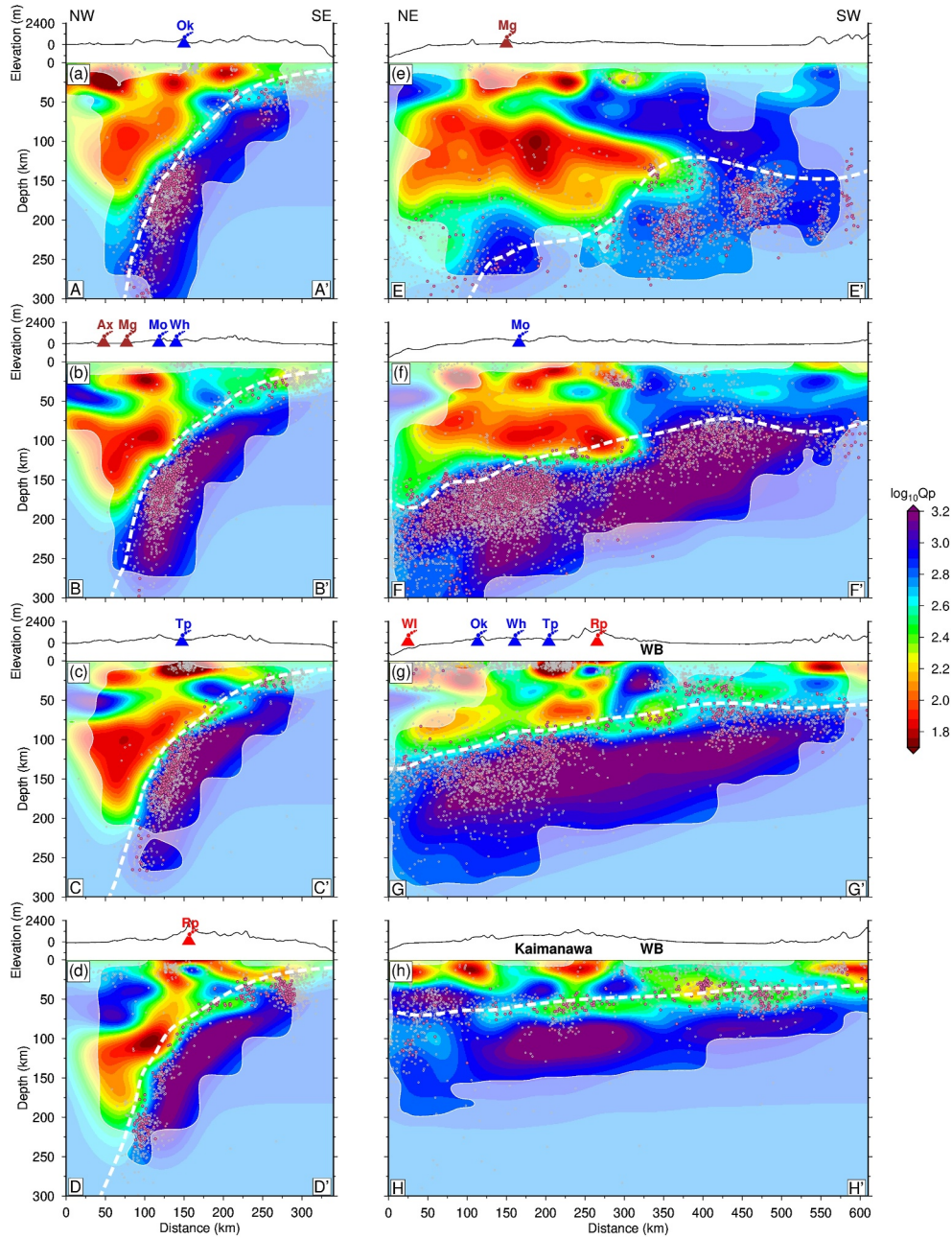

Figure 6. Trench-perpendicular and trench-parallel cross-sections through the final 3-D Q_P model. Locations of cross-sections are in Figure 5c. Gray dots represent the full seismicity within 10 km of each cross-section, while pink dots indicate the events used for inversion. White dashed lines show the plate interface model of Williams et al. (2013). The interpretable region is defined by the CRTs.

gradient at depths of 100–110 km beneath the northernmost South Island may represent the LAB (Hua et al., 2018), suggesting that the thick lithosphere may extend from the southern North Island to the northern South Island.

3.4.3. Complex Patterns of Fluid and Melt Transport in the Mantle Wedge

The position and geometry of low Q_P anomalies in the mantle wedge exhibit complex patterns (Figure 6). The most prominent feature is the extensive, low Q_P anomalies in the mantle wedge beneath the backarc region, which appear to be obliquely elongated toward the region beneath the arc. As seen in the backarc west of Okataina (Ok)

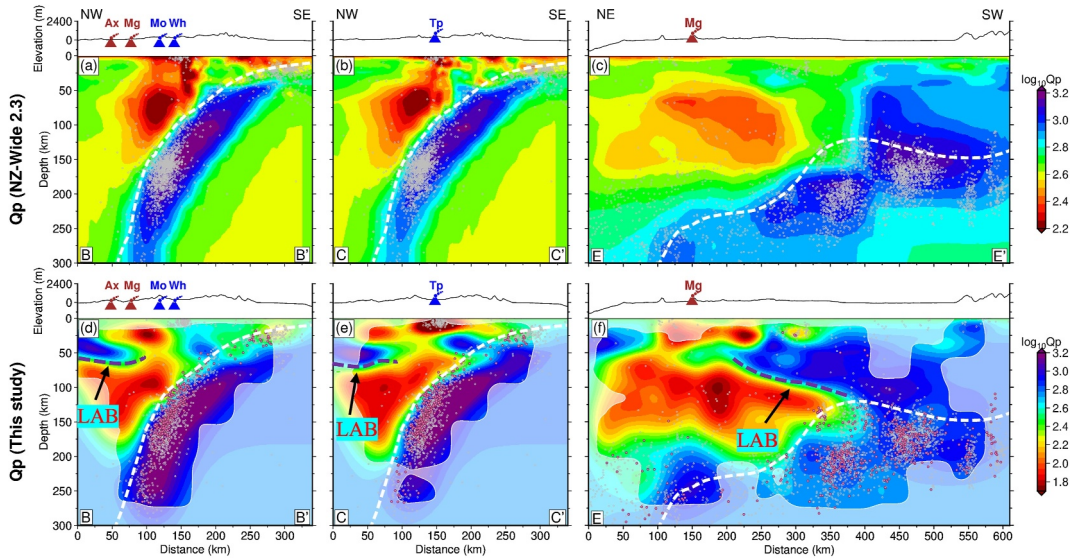

Figure 7. Comparison of the inverted 3-D Q_P model (second row) with the Q_P model (first row) from the NZ-Wide 2.3 model (Eberhart-Phillips et al., 2022) along cross-sections B-B′, C-C′ and E-E′. Locations of these cross-sections are in Figure 5c. Gray dots represent the full seismicity within 10 km of each cross-section, while pink dots indicate the events used for inversion. White dashed lines show the plate interface model of Williams et al. (2013).

(Figure 6a), Taupō (Tp) (Figure 6c), and Ruapehu (Rp) (Figure 6d), the low Q_P anomalies originate at depths of ∼175–200 km, with the upper boundary extending up to the LAB. The obliquely ascending low Q_P anomalies appear to penetrate the lithospheric mantle, reaching the crust beneath Mangakino (Mo) and Whakamaru (Wh) (Figure 6b) and extending even closer to the surface beneath Okataina, Taupō, and Ruapehu (Figures 6a, 6c, and 6d). The obliquely elongated low Q_P mantle wedge is well recovered in the restoration test (Figures 8d and 8e), indicating its reliability. Our results reveal different patterns from NZ-Wide 2.3 model, which shows low Q_P beneath the arc volcanoes, with a pronounced low Q_P anomaly occurring at depths of 50–85 km (Figures 7a and 7b). Eberhart-Phillips et al. (2008) interpret this low Q_P as indicative of the dehydration of the subducted slab, with the associated melts traveling vertically from the slab to the sub-arc crustal magma chambers. They also

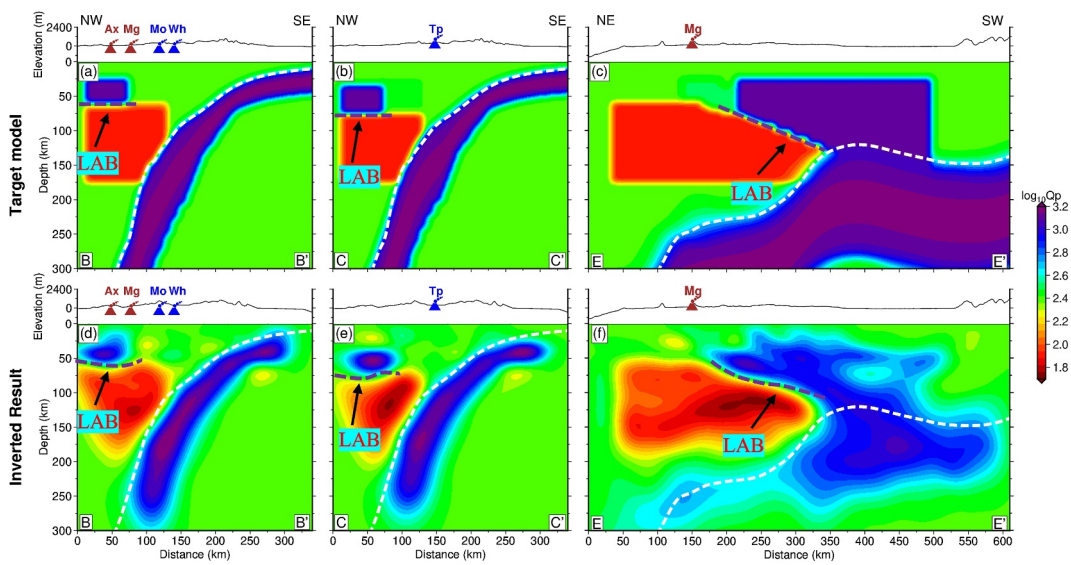

Figure 8. Comparison between the target model and the inversion results for the restoration test along cross-sections B-B′, C-C′ and E-E′. Locations of these cross-sections are in Figure 5c. White dashed lines show the plate interface model of Williams et al. (2013).

suggest that the deepest extent of low Q_P at 140 km marks the onset of hydrous melting due to chlorite breakdown within a fluid-rich, viscous blanket that thickens with the descent of the slab and is strongly coupled to the slab (Figures 7a and 7b) (Eberhart-Phillips et al., 2008).

We interpret that a high-viscosity blanket may undergo dehydration as the plate subducts deeper (>140 km), due to the existence of amphibole and phlogopite (e.g., Poli & Schmidt, 1995; Schmidt & Poli, 1998; Tatsumi, 1989). Such dehydration facilitates the down-dip transport of slab-derived fluids toward the back-arc region. The distribution of the low Q_P beneath the backarc could be a piece of evidence that melts in the mantle wedge, originating from slab-derived fluids, follow an indirect, non-vertical path before reaching the active volcanoes. Additionally, we observe a 100-km-long patch of dense slab seismicity, located at depths ranging from 125 km to over 225 km (Figures 7d and 7e). Slab earthquakes are enabled by embrittlement caused by overpressure from accumulated dehydration water, which can migrate across the slab, either updip or downdip, depending on pressure gradients and fracture permeability (e.g., Eberhart-Phillips et al., 2020; Faccenda et al., 2012). We suppose that at depths greater than 140 km, patches of the seismicity are potentially related to the deep dehydration reactions and fluid release (e.g., Eberhart-Phillips et al., 2013; Rüpke et al., 2004). The abundant seismicity at depths of 125–250 km could serve as evidence of the dehydration of the deeply subducted slab. A further question that needs to be addressed is why melts are prevented from ascending vertically through the upper plate into the backarc. This may be attributed to the low permeability, which could be induced by the low temperature of the backarc upper plate (e.g., Ha et al., 2020; Hicks et al., 2023).

Our interpretation, enlightened by the analysis of the backarc low Q_P in Lesser Antilles arc (Hicks et al., 2023), proposes an alternative model that explains the fluid pathways and melting from the slab to the arc in northern New Zealand. However, further geophysical evidence, such as v_P/v_S ratio beneath the backarc, is necessary to confirm our findings.

4. Conclusions

We propose a novel seismic attenuation tomography method based on the adjoint-state technique, called adjoint-state attenuation tomography. Compared with traditional ray-based attenuation tomography methods, the developed method has several distinct advantages. First, the cumbersome step of ray tracing can be avoided. t^* is accurately calculated using highly stable, grid-based FSM solvers. This involves first solving the Eikonal equation for the traveltime field (Zhao, 2005), followed by solving the t^* governing equation (D. Wang, Chen, Hao, & Tong, 2025), which allows for precise descriptions of the t and t^* fields in complex media, while appropriately circumventing the multipathing issue (Tong et al., 2024). Second, while calculating the Fréchet derivative of the misfit function, the inversion scheme is matrix-free, and thus we do not need to store and invert any matrix, during the optimization process. In detail, the inversion scheme primarily requires solving the forward and adjoint equations, which is approximately double the computational cost of solving the forward-modeling problem alone, thus maintaining a low computational cost (Taillandier et al., 2009).

The developed method is benchmarked by imaging the 3-D Q_P structures in Hikurangi subduction zone, northern New Zealand. The frequency-dependent t^* at 1 Hz is measured for each event-station pair, along with the simultaneous determination of the corner frequency and seismic moment for each earthquake. A total of 65,001 P-wave t^* measurements from 6,478 earthquakes recorded at 44 stations are used to invert for the Q_P structure. The inverted Q_P model is comparable to the NZ-Wide 2.3 model. The most striking characteristic of the high Q_P is associated with the subducted, cold Pacific plate, adjacent to the low Q_P mantle wedge. Our results reveal a distinct boundary beneath the back-arc at depths of ~60–100 km, characterized by contrasting high and low Q_P values, which may indicate a gradually thickening lithosphere–asthenosphere boundary (LAB) from northeast to southwest in North island. The low Q_P beneath the backarc extends from the LAB to depths of ~150–200 km, ascending obliquely toward the region beneath the arc, likely resulting from the dehydration of the deeply subducted slab.

Conflict of Interest

The authors declare no conflicts of interest relevant to this study.

Data Availability Statement

The seismic waveform data for t^* measurements are downloaded through the New Zealand permanent network (GeoNet; www.geonet.org.nz; Gale et al., 2015; Petersen et al., 2011). Figures are made by the Generic Mapping Tool (Wessel et al., 2019). The measured P-wave attenuation operator t^* data and the inverted attenuation model are available on Zenodo at https://doi.org/10.5281/zenodo.15272752 (D. Wang, Chen, Wu, et al., 2025).

Acknowledgments

We extend our gratitude to the Editor, Dr Fenglin Niu and two anonymous reviewers for their valuable and constructive comments and suggestions. We acknowledge the New Zealand GeoNet programme and its sponsors NHC, GNS Science, LINZ, NEMA and MBIE for providing data/images used in this study. We also gratefully acknowledge Stephen P. Hicks for developing the ATTENpy package, which is employed in the inversion of the data. This research is supported by the Ministry of Education, Singapore, under its MOE AcRF Tier-2 grants (MOE-T2EP20124-0003, MOE-T2EP20122-0008, and MOE-T2EP50124-0011) and Tier 1 Grant (RG86/22). SW is partly supported by the "CUG Scholar" Scientific Research Funds at China University of Geosciences (Wuhan) (Project No. 2024012) and the Fundamental Research Funds for the Central Universities, China University of Geosciences (Wuhan) (No. CUG240638). The computational work for this study was partially performed using resources provided by the National Supercomputing Centre (NSCC), Singapore (https://www.nscc.sg).

References

Abercrombie, R. E. (1995). Earthquake source scaling relationships from -1 to 5 ml using seismograms recorded at 2.5-km depth. *Journal of Geophysical Research*, *100*(B12), 24015–24036. https://doi.org/10.1029/95jb02397

Abers, G. A., Fischer, K., Hirth, G., Wiens, D., Plank, T., Holtzman, B. K., et al. (2014). Reconciling mantle attenuation-temperature relationships from seismology, petrology, and laboratory measurements. *Geochemistry, Geophysics, Geosystems*, *15*(9), 3521–3542. https://doi.org/10.1002/2014gc005444

Aki, K., & Chouet, B. (1975). Origin of coda waves: Source, attenuation, and scattering effects. *Journal of Geophysical Research*, *80*(23), 3322–3342. https://doi.org/10.1029/jb080i023p03322

Aki, K., & Richards, P. G. (2002). Quantitative seismology.

Alkhalifah, T., & Fomel, S. (2001). Implementing the fast marching eikonal solver: Spherical versus Cartesian coordinates. *Geophysical Prospecting*, *49*(2), 165–178. https://doi.org/10.1046/j.1365-2478.2001.00245.x

Anderson, J. G. (1986). Implication of attenuation for studies of the earthquake source. In *Earthquake source mechanics* (Vol. 37, pp. 311–318).

Ansell, J., & Bannister, S. (1996). Shallow morphology of the subducted Pacific plate along the Hikurangi margin, New Zealand. *Physics of the Earth and Planetary Interiors*, *93*(1–2), 3–20. https://doi.org/10.1016/0031-9201(95)03085-9

Artemieva, I. M., Billien, M., Lévêque, J.-J., & Mooney, W. D. (2004). Shear wave velocity, seismic attenuation, and thermal structure of the continental upper mantle. *Geophysical Journal International*, *157*(2), 607–628. https://doi.org/10.1111/j.1365-246x.2004.02195.x

Boatwright, J. (1978). Detailed spectral analysis of two small New York State earthquakes. *Bulletin of the Seismological Society of America*, *68*(4), 1117–1131.

Buffett, W. A., Rychert, C. A., & Harmon, N. (2025). S-to-P receiver function imaging of lithospheric discontinuities in New Zealand at the Hikurangi subduction zone. *Geochemistry, Geophysics, Geosystems*, *26*(3), e2024GC011897. https://doi.org/10.1029/2024gc011897

Chen, G., Chen, J., Li, T., Xu, M., Zhao, Q., & Tong, P. (2025). Adjoint-state reflection traveltime tomography for velocity and interface inversion with its application in central California near Parkfield. *Journal of Geophysical Research: Solid Earth*, *130*(1), e2024JB029918. https://doi.org/10.1029/2024jb029918

Chen, J., Chen, G., Nagaso, M., & Tong, P. (2023). Adjoint-state traveltime tomography for azimuthally anisotropic media in spherical coordinates. *Geophysical Journal International*, *234*(1), 712–736. https://doi.org/10.1093/gji/ggad093

Chen, J., Wu, S., Xu, M., Nagaso, M., Yao, J., Wang, K., et al. (2023). Adjoint-state teleseismic traveltime tomography: Method and application to Thailand in indochina peninsula. *Journal of Geophysical Research: Solid Earth*, *128*(12), e2023JB027348. https://doi.org/10.1029/2023jb027348

Cormier, V. F. (2020). Seismic viscoelastic attenuation. In *Encyclopedia of solid Earth geophysics* (pp. 1–14). Springer.

DeMets, C., Gordon, R. G., Argus, D. F., & Stein, S. (1994). Effect of recent revisions to the geomagnetic reversal time scale on estimates of current plate motions. *Geophysical Research Letters*, *21*(20), 2191–2194. https://doi.org/10.1029/94gl02118

Dimech, J.-L., Stern, T., & Lamb, S. (2017). Mantle earthquakes, crustal structure, and gravitational instability beneath western North Island, New Zealand. *Geology*, *45*(2), 155–158. https://doi.org/10.1130/g38476.1

Eberhart-Phillips, D., Bannister, S., & Ellis, S. (2014). Imaging p and s attenuation in the termination region of the Hikurangi Subduction Zone, New Zealand. *Geophysical Journal International*, *198*(1), 516–536. https://doi.org/10.1093/gji/ggu151

Eberhart-Phillips, D., Bannister, S., & Reyners, M. (2020). Attenuation in the mantle wedge beneath super-volcanoes of the Taupo Volcanic Zone, New Zealand. *Geophysical Journal International*, *220*(1), 703–723. https://doi.org/10.1093/gji/ggz455

Eberhart-Phillips, D., Bannister, S., Reyners, M., & Bourguignon, S. (2022). New Zealand wide model 2.3 seismic velocity model for New Zealand (vlnzwide2.3) [Dataset]. *Zenodo*. https://doi.org/10.5281/zenodo.6568301

Eberhart-Phillips, D., & Chadwick, M. (2002). Three-dimensional attenuation model of the shallow Hikurangi subduction zone in the Raukumara Peninsula, New Zealand. *Journal of Geophysical Research*, *107*(B2), ESE3-1–ESE3-15. https://doi.org/10.1029/2000jb000046

Eberhart-Phillips, D., Reyners, M., Chadwick, M., & Stuart, G. (2008). Three-dimensional attenuation structure of the Hikurangi subduction zone in the central North Island, New Zealand. *Geophysical Journal International*, *174*(1), 418–434. https://doi.org/10.1111/j.1365-246x.2008.03816.x

Eberhart-Phillips, D., Reyners, M., Faccenda, M., & Naliboff, J. (2013). Along-strike variation in subducting plate seismicity and mantle wedge attenuation related to fluid release beneath the North Island, New Zealand. *Physics of the Earth and Planetary Interiors*, *225*, 12–27. https://doi.org/10.1016/j.pepi.2013.10.002

Faccenda, M., Gerya, T. V., Mancktelow, N. S., & Moresi, L. (2012). Fluid flow during slab unbending and dehydration: Implications for intermediate-depth seismicity, slab weakening and deep water recycling. *Geochemistry, Geophysics, Geosystems*, *13*(1). https://doi.org/10.1029/2011gc003860

Farrokhi, M., Hamzehloo, H., Rahimi, H., & Zadeh, M. A. (2016). Separation of intrinsic and scattering attenuation in the crust of central and eastern Alborz Region, Iran. *Physics of the Earth and Planetary Interiors*, *253*, 88–96. https://doi.org/10.1016/j.pepi.2016.02.005

Fichtner, A., Bunge, H.-P., & Igel, H. (2006). The adjoint method in seismology: I. theory. *Physics of the Earth and Planetary Interiors*, *157*(1–2), 86–104. https://doi.org/10.1016/j.pepi.2006.03.016

Frankel, A., & Wennerberg, L. (1987). Energy-flux model of seismic coda: Separation of scattering and intrinsic attenuation. *Bulletin of the Seismological Society of America*, *77*(4), 1223–1251. https://doi.org/10.1785/bssa0770041223

Gale, N., Gledhill, K., Chadwick, M., & Wallace, L. (2015). The Hikurangi margin continuous GNSS and seismograph network of New Zealand. *Seismological Research Letters*, *86*(1), 101–108. https://doi.org/10.1785/0220130181

GNS Science. (1970). GeoNet Aotearoa New Zealand earthquake catalogue [Dataset]. *GNS Science, GeoNet*. https://doi.org/10.21420/0S8P-TZ38

Ha, G., Montési, L. G., & Zhu, W. (2020). Melt focusing along permeability barriers at subduction zones and the location of volcanic arcs. *Geochemistry, Geophysics, Geosystems*, *21*(12), e2020GC009253. https://doi.org/10.1029/2020gc009253

Hao, S., Chen, J., Xu, M., & Tong, P. (2024). Topography-incorporated adjoint-state surface wave traveltime tomography: Method and a case study in Hawaii. *Journal of Geophysical Research: Solid Earth*, *129*(1), e2023JB027454. https://doi.org/10.1029/2023jb027454

Hicks, S. P., Bie, L., Rychert, C. A., Harmon, N., Goes, S., Rietbrock, A., et al. (2023). Slab to back-arc to arc: Fluid and melt pathways through the mantle wedge beneath the lesser Antilles. *Science Advances*, *9*(5), eadd2143. https://doi.org/10.1126/sciadv.add2143

Horspool, N., Savage, M., & Bannister, S. (2006). Implications for intraplate volcanism and back-arc deformation in northwestern New Zealand, from joint inversion of receiver functions and surface waves. *Geophysical Journal International*, *166*(3), 1466–1483. https://doi.org/10.1111/j.1365-246x.2006.03016.x

Hua, J., Fischer, K. M., & Savage, M. K. (2018). The lithosphere–asthenosphere boundary beneath the south island of New Zealand. *Earth and Planetary Science Letters*, *484*, 92–102. https://doi.org/10.1016/j.epsl.2017.12.011

Huang, J.-W., & Bellefleur, G. (2012). Joint transmission and reflection traveltime tomography using the fast sweeping method and the adjoint-state technique. *Geophysical Journal International*, *188*(2), 570–582. https://doi.org/10.1111/j.1365-246x.2011.05273.x

Huang, X., Guo, Z., Zhou, H., & Yue, Y. (2020). First arrival Q tomography based on an adjoint-state method. *Journal of Geophysics and Engineering*, *17*(4), 577–591. https://doi.org/10.1093/jge/gxaa008

Jackson, I., & Faul, U. H. (2010). Grainsize-sensitive viscoelastic relaxation in olivine: Towards a robust laboratory-based model for seismological application. *Physics of the Earth and Planetary Interiors*, *183*(1–2), 151–163. https://doi.org/10.1016/j.pepi.2010.09.005

Jackson, I., Fitz Gerald, J. D., Faul, U. H., & Tan, B. H. (2002). Grain-size-sensitive seismic wave attenuation in polycrystalline olivine. *Journal of Geophysical Research*, *107*(B12), ECV5-1–ECV5-16. https://doi.org/10.1029/2001jb001225

Karaoğlu, H., & Romanowicz, B. (2018). Inferring global upper-mantle shear attenuation structure by waveform tomography using the spectral element method. *Geophysical Journal International*, *213*(3), 1536–1558. https://doi.org/10.1093/gji/ggy030

Keers, H., Vasco, D. W., & Johnson, L. R. (2001). Viscoacoustic crosswell imaging using asymptotic waveforms. *Geophysics*, *66*(3), 861–870. https://doi.org/10.1190/1.1444975

Koketsu, K., & Sekine, S. (1998). Pseudo-bending method for three-dimensional seismic ray tracing in a spherical Earth with discontinuities. *Geophysical Journal International*, *132*(2), 339–346. https://doi.org/10.1046/j.1365-246x.1998.00427.x

Kravtsov, Y. A., & Orlov, Y. I. (1990). *Geometrical optics of inhomogeneous media* (Vol. 38). Springer.

Lees, J. M., & Lindley, G. T. (1994). Three-dimensional attenuation tomography at Loma Prieta: Inversion of t* for Q. *Journal of Geophysical Research*, *99*(B4), 6843–6863. https://doi.org/10.1029/93jb03460

Leung, S., & Qian, J. (2006). An adjoint state method for three-dimensional transmission traveltime tomography using first-arrivals. *Communications in Mathematical Sciences*, *4*(1), 249–266. https://doi.org/10.4310/cms.2006.v4.n1.a10

Lindley, G. T., & Archuleta, R. J. (1992). Earthquake source parameters and the frequency dependence of attenuation at Coalinga, Mammoth Lakes, and the Santa Cruz Mountains, California. *Journal of Geophysical Research*, *97*(B10), 14137–14154. https://doi.org/10.1029/92jb00550

Liu, X., & Zhao, D. (2015). Seismic attenuation tomography of the southwest Japan arc: New insight into subduction dynamics. *Geophysical Journal International*, *201*(1), 135–156. https://doi.org/10.1093/gji/ggv007

Liu, X., Zhao, D., & Li, S. (2014). Seismic attenuation tomography of the northeast Japan arc: Insight into the 2011 Tohoku earthquake (Mw 9.0) and subduction dynamics. *Journal of Geophysical Research: Solid Earth*, *119*(2), 1094–1118. https://doi.org/10.1002/2013jb010591

Mortimer, N. (2004). New Zealand's geological foundations. *Gondwana Research*, *7*(1), 261–272. https://doi.org/10.1016/s1342-937x(05)70324-5

Nakajima, J., Hada, S., Hayami, E., Uchida, N., Hasegawa, A., Yoshioka, S., et al. (2013). Seismic attenuation beneath northeastern Japan: Constraints on mantle dynamics and arc magmatism. *Journal of Geophysical Research: Solid Earth*, *118*(11), 5838–5855. https://doi.org/10.1002/2013jb010388

Petersen, T., Gledhill, K., Chadwick, M., Gale, N. H., & Ristau, J. (2011). The New Zealand national seismograph network. *Seismological Research Letters*, *82*(1), 9–20. https://doi.org/10.1785/gssrl.82.1.9

Plessix, R.-E., Mulder, W., & Ten Kroode, A. (2000). Automatic cross-well tomography by semblance and differential semblance optimization: Theory and gradient computation. *Geophysical Prospecting*, *48*(5), 913–935. https://doi.org/10.1046/j.1365-2478.2000.00217.x

Poli, S., & Schmidt, M. W. (1995). H_2O transport and release in subduction zones: Experimental constraints on basaltic and andesitic systems. *Journal of Geophysical Research*, *100*(B11), 22299–22314. https://doi.org/10.1029/95jb01570

Pozgay, S. H., Wiens, D. A., Conder, J. A., Shiobara, H., & Sugioka, H. (2009). Seismic attenuation tomography of the Mariana subduction system: Implications for thermal structure, volatile distribution, and slow spreading dynamics. *Geochemistry, Geophysics, Geosystems*, *10*(4). https://doi.org/10.1029/2008gc002313

Prieto, G. A. (2022). The multitaper spectrum analysis package in Python. *Seismological Society of America*, *93*(3), 1922–1929. https://doi.org/10.1785/0220210332

Rawlinson, N., Hauser, J., & Sambridge, M. (2008). Seismic ray tracing and wavefront tracking in laterally heterogeneous media. *Advances in Geophysics*, *49*, 203–273. https://doi.org/10.1016/s0065-2687(07)49003-3

Rawlinson, N., Pozgay, S., & Fishwick, S. (2010). Seismic tomography: A window into deep Earth. *Physics of the Earth and Planetary Interiors*, *178*(3–4), 101–135. https://doi.org/10.1016/j.pepi.2009.10.002

Rawlinson, N., & Sambridge, M. (2004). Wave front evolution in strongly heterogeneous layered media using the fast marching method. *Geophysical Journal International*, *156*(3), 631–647. https://doi.org/10.1111/j.1365-246x.2004.02153.x

Ristau, J. (2013). Update of regional moment tensor analysis for earthquakes in New Zealand and adjacent offshore regions. *Bulletin of the Seismological Society of America*, *103*(4), 2520–2533. https://doi.org/10.1785/0120120339

Romanowicz, B., & Mitchell, B. (2015). 1.25: Deep Earth structure: Q of the Earth from crust to core. *Treatise on Geophysics*, *1*, 789–827.

Rüpke, L. H., Morgan, J. P., Hort, M., & Connolly, J. A. (2004). Serpentine and the subduction zone water cycle. *Earth and Planetary Science Letters*, *223*(1–2), 17–34. https://doi.org/10.1016/j.epsl.2004.04.018

Rychert, C. A., Fischer, K. M., Abers, G. A., Plank, T., Syracuse, E., Protti, J., et al. (2008). Strong along-arc variations in attenuation in the mantle wedge beneath Costa Rica and Nicaragua. *Geochemistry, Geophysics, Geosystems*, *9*(10). https://doi.org/10.1029/2008gc002040

Sato, H., Fehler, M. C., & Maeda, T. (2012). *Seismic wave propagation and scattering in the heterogeneous Earth* (Vol. 496). Springer.

Schlotterbeck, B. A., & Abers, G. A. (2001). Three-dimensional attenuation variations in southern California. *Journal of Geophysical Research*, *106*(B12), 30719–30735. https://doi.org/10.1029/2001jb000237

Schmidt, M. W., & Poli, S. (1998). Experimentally based water budgets for dehydrating slabs and consequences for arc magma generation. *Earth and Planetary Science Letters*, *163*(1–4), 361–379. https://doi.org/10.1016/s0012-821x(98)00142-3

Shearer, P. M. (2019). *Introduction to seismology*. Cambridge University Press.

Stachnik, J. C., Abers, G. A., & Christensen, D. H. (2004). Seismic attenuation and mantle wedge temperatures in the Alaska subduction zone. *Journal of Geophysical Research*, *109*(B10). https://doi.org/10.1029/2004jb003018

Stern, T., Houseman, G., Salmon, M., & Evans, L. (2013). Instability of a lithospheric step beneath western North Island, New Zealand. *Geology*, *41*(4), 423–426. https://doi.org/10.1130/g34028.1

Taillandier, C., Noble, M., Chauris, H., & Calandra, H. (2009). First-arrival traveltime tomography based on the adjoint-state method. *Geophysics*, *74*(6), WCB1–WCB10. https://doi.org/10.1190/1.3250266

Tarantola, A. (1984). Inversion of seismic reflection data in the acoustic approximation. *Geophysics*, *49*(8), 1259–1266. https://doi.org/10.1190/1.1441754

Tatsumi, Y. (1989). Migration of fluid phases and genesis of basalt magmas in subduction zones. *Journal of Geophysical Research*, *94*(B4), 4697–4707. https://doi.org/10.1029/jb094ib04p04697

Tavakoli, F. B., Operto, S., Ribodetti, A., & Virieux, J. (2017). Slope tomography based on eikonal solvers and the adjoint-state method. *Geophysical Journal International*, *209*(3), 1629–1647. https://doi.org/10.1093/gji/ggx111

Tong, P. (2021a). Adjoint-state traveltime tomography: Eikonal equation-based methods and application to the Anza Area in southern California. *Journal of Geophysical Research: Solid Earth*, *126*(5), e2021JB021818. https://doi.org/10.1029/2021jb021818

Tong, P. (2021b). Adjoint-state traveltime tomography for azimuthally anisotropic media and insight into the crustal structure of central California near Parkfield. *Journal of Geophysical Research: Solid Earth*, *126*(10), e2021JB022365. https://doi.org/10.1029/2021jb022365

Tong, P., Li, T., Chen, J., & Nagaso, M. (2024). Adjoint-state differential arrival time tomography. *Geophysical Journal International*, *236*(1), 139–160. https://doi.org/10.1093/gji/ggad416

Tong, P., Yang, D., & Huang, X. (2019). Multiple-grid model parametrization for seismic tomography with application to the San Jacinto Fault Zone. *Geophysical Journal International*, *218*(1), 200–223. https://doi.org/10.1093/gji/ggz151

Tromp, J., Tape, C., & Liu, Q. (2005). Seismic tomography, adjoint methods, time reversal and banana-doughnut kernels. *Geophysical Journal International*, *160*(1), 195–216. https://doi.org/10.1111/j.1365-246x.2004.02453.x

Um, J., & Thurber, C. (1987). A fast algorithm for two-point seismic ray tracing. *Bulletin of the Seismological Society of America*, *77*(3), 972–986. https://doi.org/10.1785/bssa0770030972

Wang, D., Chen, J., Hao, S., & Tong, P. (2025). A novel fast sweeping method for computing the attenuation operator t* in absorbing media. *Geophysical Journal International*, *243*(3). https://doi.org/10.1093/gji/ggaf381

Wang, D., Chen, J., Wu, S., Li, T., Bai, Y., Gao, Y., & Tong, P. (2025). Adjoint-state attenuation tomography: Method and application to north New Zealand [Model] [Dataset]. *Zenodo*. https://doi.org/10.5281/zenodo.15272752

Wang, N., Yang, D., Shen, Y., Bao, X., & Li, J. (2023). 3d sensitivity kernels with full attenuation computed by a combination of the strong stability preserving Runge-Kutta method and the scattering-integral method. *Journal of Geophysical Research: Solid Earth*, *128*(8), e2023JB026808. https://doi.org/10.1029/2023jb026808

Wang, Z., & Zhao, D. (2019). Updated attenuation tomography of Japan subduction zone. *Geophysical Journal International*, *219*(3), 1679–1697. https://doi.org/10.1093/gji/ggz339

Wei, S. S., & Wiens, D. A. (2018). P-wave attenuation structure of the Lau back-arc basin and implications for mantle wedge processes. *Earth and Planetary Science Letters*, *502*, 187–199. https://doi.org/10.1016/j.epsl.2018.09.005

Wessel, P., Luis, J. F., Uieda, L. A., Scharroo, R., Wobbe, F., Smith, W. H., & Tian, D. (2019). The generic mapping tools version 6. *Geochemistry, Geophysics, Geosystems*, *20*(11), 5556–5564. https://doi.org/10.1029/2019gc008515

Wiens, D. A., Conder, J. A., & Faul, U. H. (2008). The seismic structure and dynamics of the mantle wedge. *Annual Review of Earth and Planetary Sciences*, *36*(1), 421–455. https://doi.org/10.1146/annurev.earth.33.092203.122633

Williams, C. A., Eberhart-Phillips, D., Bannister, S., Barker, D. H., Henrys, S., Reyners, M., & Sutherland, R. (2013). Revised interface geometry for the Hikurangi Subduction Zone, New Zealand. *Seismological Research Letters*, *84*(6), 1066–1073. https://doi.org/10.1785/0220130035

Wilson, C., Houghton, B., McWilliams, M., Lanphere, M. A., Weaver, S., & Briggs, R. (1995). Volcanic and structural evolution of Taupo Volcanic Zone, New Zealand: A review. *Journal of Volcanology and Geothermal Research*, *68*(1–3), 1–28. https://doi.org/10.1016/0377-0273(95)00006-g

Zhao, H. (2005). A fast sweeping method for eikonal equations. *Mathematics of Computation*, *74*(250), 603–627. https://doi.org/10.1090/s0025-5718-04-01678-3

Zhu, H., Bozdağ, E., Duffy, T. S., & Tromp, J. (2013). Seismic attenuation beneath Europe and the north Atlantic: Implications for water in the mantle. *Earth and Planetary Science Letters*, *381*, 1–11. https://doi.org/10.1016/j.epsl.2013.08.030